

# Estimating Monthly Global Ground-Level NO<sub>2</sub> Concentrations Using Geographically Weighted Panel Regression

## Abstract

Predicting long-term ground-level nitrogen dioxide (NO<sub>2</sub>) is important globally to support environmental and public health research and to provide information to governments and society for air pollution control policies. The ozone monitoring instrument (OMI), using Aura Satellite, detects monthly global tropospheric column amounts (TrCA) of NO<sub>2</sub> molecules. However, the relationship between the ground-level NO<sub>2</sub> concentration and TrCA of NO<sub>2</sub> molecules remains elusive because NO<sub>2</sub> molecules in the air are not vertically evenly distributed. Here, we examine the relationship between satellite-derived data and measured ground-level NO<sub>2</sub> concentration, controlling several meteorological variables from January 2015 to October 2021. The geographically weighted panel regression (GWPR) is built and applied. The accuracy of GWPR prediction is 69.61%. The coefficient of correlation between predicted and measure value is 0.8376. The root mean square error and mean absolute error are 7.84 and 4.07  $\mu\text{g}/\text{m}^3$ , respectively. Moreover, the GWPR is the reliable indicated by the 10-fold cross-validation. The GWPR can analyze unbalanced panel data and capture the spatial variability of the relationship. Based on the GWPR estimation, the 82 monthly global ground-level NO<sub>2</sub> concentrations are predicted from January 2015 to October 2021. Overall, this research provides critical

basic data to environmental and public health science and valuable information for governments and societies to make more reasonable policies.

## Keywords

Monthly Ground-Level NO<sub>2</sub> Concentration; GWPR model; spatial non-stationarity; OMI

## Introduction

Air pollutant, nitrogen dioxide (NO<sub>2</sub>), is adversely related to various health outcomes (Lelieveld et al. 2015; Newell et al. 2017; Ogen 2020; Orellano et al. 2020). The relationship between all-cause mortality and NO<sub>2</sub> concentration is positive (Brunekreef and Holgate 2002). Specifically, a 10  $\mu\text{g}/\text{m}^3$  increase in NO<sub>2</sub> concentration in short-term is associated with a 0.72% increase in the relative risks of all-cause mortality (Orellano et al. 2020). The European Union and World Health Organization (WHO) recommend that the annual average exposure to ambient NO<sub>2</sub> should be lower than 40  $\mu\text{g}/\text{m}^3$ . Additionally, other air pollutants, such as particulate matter and ozone, are related to approximately 3.3 million premature deaths per year globally, and NO<sub>2</sub> is one of the critical factors attributable to these pollutants (Beckerman et al. 2008; Lelieveld et al. 2015). Evidence shows a link between NO<sub>2</sub> and various acute and chronic diseases, especially decreased lung function and lung cancer (Chiusolo et al. 2011; Hamra et al. 2015; Rice et al. 2013). Furthermore, several studies indicate that in areas with high NO<sub>2</sub> concentration, people are

more easily infected by the coronavirus and more difficult to recover (Li and Managi 2022; Ogen 2020; Wu et al. 2020; Yao et al. 2021). Besides, air pollution affects human well-being directly (Li and Managi 2021). For Example, a  $10 \mu\text{g}/\text{m}^3$  in annual average  $\text{NO}_2$  is related to a roughly 50% decrease of life satisfaction, in London (Mackerron and Mourato 2009). The ground-level  $\text{NO}_2$  concentration affects human well-being and public health the most (Lelieveld et al. 2015; Li and Managi 2021, 2022). However, the satellite instrument, the Ozone Monitoring Instrument (OMI), focuses mainly on the tropospheric column amounts (TrCA) and the total column amounts (ToCA) of  $\text{NO}_2$  (OMI Team 2012). The association ground-level  $\text{NO}_2$  concentration with TrCA or ToCA remains unclear because the  $\text{NO}_2$  molecules are not vertically evenly distributed in the air. Besides, there is a lack of ground-level  $\text{NO}_2$  concentration measurements in low-income countries, which induces broad uncertainty of ground-level  $\text{NO}_2$  distribution (Larkin et al. 2017). In order to help to detect the adverse impacts of  $\text{NO}_2$  on public health and human well-being, the global time-series ground-level  $\text{NO}_2$  data is strongly desired.

Geographically weighted regression (GWR) is an advanced method that estimates air pollution taking the spatial contexts into account (Bigdeli et al. 2021; Jiang et al. 2017). To examine the relationship between satellite-derived data and measured ground-level air pollution, a variety of models are developed, such as land-use regression (Bechle et al. 2015; Larkin et al. 2017), chemical transport model (Geddes et al. 2016), linear regression model (Lin et al. 2019; Liu et al. 2017), GIS-based multi-source and multi-box model (Wang and Chen 2013), geographically and temporally weighted regression (Li et al. 2020; Qin et al. 2017), among others (Kim et al. 2021). However, there is still space to improve the accuracy of these models. Most of these models are global and do not fully take spatial

variability of the relationship between satellite-derived data and measured ground-level air pollution into account. In other words, the association is spatially stationary and does not change with spatial context (Hu et al. 2013; Song et al. 2014). The GWR can illustrate the spatial variability of the relationship according to the local regression technique (Fotheringham and Oshan 2016; Hu et al. 2013).

Currently, the GWR can only analyze the cross-sectional data or the panel data by using pooled ordinary least squares (POLS). To incorporate the temporal effect into the analysis, there are two other advanced methods, GTWR (Fotheringham et al. 2015; Qin et al. 2017) and geographically weighted panel regression (GWPR) (Yu et al. 2021), to regress the balanced panel data. However, neither of these two methods can solve the problem with unbalanced panel data due to the issues in the spatially weighted matrix. In this study, the measured ground-level data is an unbalanced panel data of 530 cities from 2015 to 2021. To solve this problem, we build a new R package, “GWPR.light”, and release it on CRAN (The Comprehensive R Archive Network).

In this paper, firstly, according to a series of statistical tests and model comparisons, the GWPR with fixed time-fixed effects is preferred. This GWPR model excels at accuracy. Secondly, several auxiliary variables, including terrain atmospheric pressure, land surface temperature, normalized difference vegetation index (NDVI), precipitation, planetary boundary layer height (PBLH), and year dummy variables, are involved in the analysis to detect the relationship between ground-level and TrCA of NO<sub>2</sub>. Thirdly, the optimal bandwidth is calibrated, critical to building the spatially weighted matrix. Fourthly, the GWPR estimation is obtained and converted into raster data through the interpolation

method. Finally, the monthly global ground-level NO<sub>2</sub> concentration from January 2015 to October 2021 is provided, and the prediction accuracy is calculated.

## Materials and Methodology

### *Materials*

#### *Satellite-Derived NO<sub>2</sub> Estimation*

Vertical column amounts of NO<sub>2</sub> are provided by a satellite instrument, OMI. The OMI/Aura NO<sub>2</sub> Total and Tropospheric Column Daily L2 Global Gridded 0.25 degree × 0.25 degree V3 (OMNO2G) is the global daily grids data set with a 0.25-degree resolution to gauge TrCA and ToCA of NO<sub>2</sub> based on the observation of the NASA Earth Observing System (EOS) Aura satellite platform (Irie et al. 2012; Li and Wu 2021; Nickolay et al. 2019) ([https://disc.gsfc.nasa.gov/datasets/OMNO2G\\_003/summary](https://disc.gsfc.nasa.gov/datasets/OMNO2G_003/summary)). This satellite was launched on July 15<sup>th</sup> 2004 and began providing daily global TrCA, stratospheric column amounts and ToCA of NO<sub>2</sub> observation (unit: *molecules/cm<sup>2</sup>*) from October 1<sup>st</sup> 2004 (Nickolay et al. 2019; OMI Team 2012). The OMI-NO<sub>2</sub> data sets, especially the OMNO2G, have been widely used in emission and pollution monitoring (Curier et al. 2014; Li and Wu 2021; Liu et al. 2017). Air pollution near the ground impacts human health and daily life the most harmfully (**Figure 1**) (Hamra et al. 2015; Rice et al. 2013). However, the ground-level NO<sub>2</sub> concentration is unavailable in many areas, particularly in rural areas and most developing countries. Therefore, the conversion or the estimation from TrCA or ToCA to ground-level data becomes a critical point. The EOS Aura orbit is a sun-synchronous polar orbit at an altitude of 705 km, and the satellite goes over each location between the local

time 12:00 and 15:00 (OMI Team 2012; Schoeberl et al. 2006). Due to the orbit altitude, the ToCA of NO<sub>2</sub> covers the NO<sub>2</sub> molecules in the troposphere, stratosphere, mesosphere, and thermosphere, while TrCA of NO<sub>2</sub> takes those in only the troposphere into account. Because the troposphere is most affected by human activities and air pollution, there has the most substantial impact on human health (Lelieveld et al. 2015; Li and Managi 2022) and well-being (Li and Managi 2021), the TrCA of NO<sub>2</sub> is an ideal independent variable to predict the ground-level NO<sub>2</sub> concentration. However, owing to anthropogenic climate change, tropopause height is slowly rising (Meng et al. 2021). Though this continuous rise is relatively tiny in comparison to the tropopause height, whether it influences the estimation of the TrCA of NO<sub>2</sub> remains elusive. In order to choose the satellite NO<sub>2</sub> variable, we put both the ToCA and TrCA of NO<sub>2</sub> in the analyses as the primary variable, respectively. Both the goodness of fit of the model taking the TrCA of NO<sub>2</sub> as the dependent variable ( $R^2$ : 0.7445) and cross validation results are slightly better than the other model using the ToCA of NO<sub>2</sub> ( $R^2$ : 0.7439). Therefore, the TrCA of NO<sub>2</sub> is employed in the final analysis.

The unit of the TrCA of NO<sub>2</sub> (*molecules/cm<sup>2</sup>*) is converted in microgram per square meter ( $\mu\text{g}/\text{m}^2$ ) based on simple mathematics, to make it understandable to the public:

$$ATrCA = RTrCA/N_A \times MM_{NO_2} \times 10,000 \text{ cm}^2/\text{m}^2 \times 1,000,000 \mu\text{g}/\text{g} \quad (1)$$

where *ATrCA* is the TrCA of NO<sub>2</sub> after the unit conversion, whose unit is  $\mu\text{g}/\text{m}^2$ , *RTrCA* is the value extracted from the OMNO2G directly, whose unit is *molecules/cm<sup>2</sup>*,  $N_A$  is the Avogadro constant ( $6.022,140,857 \cdot 10^{23} \text{ mol}^{-1}$ ), and  $MM_{NO_2}$  is the molar mass of NO<sub>2</sub> (46.006,6 *g/mol*).

The temporal resolution of our analysis is monthly, although both the OMNO2G and ground-level measurements are seemingly daily. Due to the orbit height of the EOS Aura, the satellite revisit period is 16 days (Schoeberl et al. 2006). In other words, each location could at most be observed twice in a month rather than every day. Furthermore, other auxiliary satellite data, such as land surface temperature, NDVI, among others, are obtained from EOS Terra and Aqua satellites, whose satellite revisit periods are also 16 days. For these reasons, we convert the daily TrCA of NO<sub>2</sub> from the OMNO2G data set into the monthly average TrCA of NO<sub>2</sub>.

*Figure 1 is located here.*

#### *Ground-Level NO<sub>2</sub> Measurements*

Globally, daily ground-level NO<sub>2</sub> of 530 major cities has been measured from 2015. Initially, there were 539 cities included, but nine were dropped, owing to its no more than five monthly records from January 2015 to October 2021. Because the data are from the measurements of different governments and organizations, the units of measured value are not the same. In order to make them comparable, the data provider, the World Air Quality Project, has converted into the unified unit, part per billion (PPB), in accordance with the requirement of the United States Environmental Protection Agency. This data set can be downloaded from the Air Quality Open Data Platform ([https://aqicn.org/data-](https://aqicn.org/data-platform/covid19/)  
[platform/covid19/](https://aqicn.org/data-platform/covid19/)). In this study, the monthly average NO<sub>2</sub> concentration is utilized, calculated from the daily data, to merge with the satellite data correctly. The locations of the cities with measurement points are also provided by the Air Quality Open Data Platform (<https://aqicn.org/data-platform/covid19/airquality-covid19-cities.json>), shown

in **Figure 2**. In most cities, there are generally several measurement points. In the data set, the medians of ground-level NO<sub>2</sub> are recorded in view of the data from different measurement points in a specific city. The ground-level measured NO<sub>2</sub> concentration data are daily. To connect them with the satellite data, we convert them into monthly average values.

*Figure 2 is located here.*

The unit of monthly average ground-level measured NO<sub>2</sub> concentration data is PPB, while the units the monthly average TrCA of NO<sub>2</sub> is microgram per square meter ( $\mu g/m^2$ ). To make the units of these two data sets consistent, we convert the unit of monthly average ground-level measured NO<sub>2</sub> concentration data, PPB, into  $\mu g/m^3$ , based on other auxiliary variables, including terrain atmospheric pressure and temperature:

$$GNO2 = \frac{P \times MW_{NO2} \times RGNO2}{R \times T \times 1000} \quad (2)$$

where  $GNO2$  is the monthly average ground-level NO<sub>2</sub> concentration, whose unit is  $\mu g/m^3$ ,  $RGNO2$  is the NO<sub>2</sub> concentration before conversion, whose unit is PPB,  $P$  is the terrain atmospheric pressure (mmHg), which could be extracted from OMNO2G and converted into the monthly average values (OMNO2G data unit is hPa, and the conversion coefficient between mmHg and hPa is  $0.750,06 \text{ mmHg/hPa}$ ),  $MW_{NO2}$  is 46.0066,  $R$  is the ideal gas constant ( $62.4 \text{ L} \cdot \text{Torr} \cdot K^{-1} \cdot \text{mol}^{-1}$ ), and  $T$  is the monthly average temperature from MODIS product, MOD11C3.



## *Auxiliary Data*

Auxiliary data, including terrain atmospheric pressure, temperature, NDVI, precipitation, and PBLH, are taken as the control variables to improve the model's performance. Terrain atmospheric pressure is involved in the analyses of NO<sub>2</sub> concentration in a considerable amount of previous studies (Chi et al. 2021; Li et al. 2020). Terrain atmospheric pressure data are acquired from OMNO2G, with a 0.25-arc-degree resolution. Although the temporal resolution of this data set is daily, but it has the same problem as the TrCA of NO<sub>2</sub> data set, a long satellite revisit period. So, we convert it into a monthly average value. Additionally, to make the calculation understandable, the unit of land surface temperature has been converted into Celsius.

The temperature data are provided by the Moderate Resolution Imaging Spectroradiometer (MODIS, <https://modis.gsfc.nasa.gov/>). The products, MOD11C3 and MYD11C3, are based on the MODIS Terra and Aqua satellites' observations and measurements, including the day-time and nighttime average temperature, with a 0.05-arc-degree spatial resolution (<https://modis.gsfc.nasa.gov/data/dataproduct/mod11.php>). Due to the 16-day revisit period, there are one or two global rasters based on each satellite's observation every month. In a month, we take the mean of all the rasters, involving the day-time and nighttime average temperature in a month to obtain the monthly average temperature raster. Of note, the spatial resolution of the monthly average temperature raster is still 0.05 arc degree. To make it consistent with the monthly average TrCA of NO<sub>2</sub>, we reduce the resolution to 0.25 arc degree, by applying the average value. The monthly NDVI data are acquired from the MODIS products, MOD13C2 and MYD13C2 (<https://modis.gsfc.nasa.gov/data/dataproduct/mod13.php>), with a 0.05-arc-degree spatial

resolution. We also use the average value to make its resolution become 0.25 arc degree.  
The NVDI value ranges from -1 to 1.

The precipitation data are obtained from NASA Global Land Data Assimilation System Version 2 (GLDAS) Noah Land Surface Model L4 monthly 0.25 x 0.25 degree V2.1 (GLDAS\_NOAH025\_M, [https://disc.gsfc.nasa.gov/datasets/GLDAS\\_NOAH025\\_M\\_2.1/summary](https://disc.gsfc.nasa.gov/datasets/GLDAS_NOAH025_M_2.1/summary)). The temporal and spatial resolutions are one month and 0.25 arc degree, respectively. This data set has some missing values because some regions are too close to the seas and oceans. To avoid the reduction of the data size in our calculation, we impute the missing values by averaging their closest surrounding grids. We estimate the data set twice, that is, the original GLDAS\_NOAH025\_M data set boundary extends roughly 0.5 arc degree into the seas and oceans. The original unit of this data set is  $kg/(m^2 \cdot s)$ , but the most values are less than  $0.0001 kg/(m^2 \cdot s)$ . To improve the readability and robustness of the calculation, we convert its unit into  $kg/(m^2 \cdot h)$ .

The PBLH data are extracted from Monthly mean, Time-Averaged, Single-Level, Assimilation, Surface Flux Diagnostics V5.12.4 (M2TMNXFLX, [https://disc.gsfc.nasa.gov/datasets/M2TMNXFLX\\_5.12.4/summary](https://disc.gsfc.nasa.gov/datasets/M2TMNXFLX_5.12.4/summary)). The spatial resolution of this data set is  $0.5^\circ \times 0.625^\circ$ . We employ the bilinear interpolation method to impute a new data set with a 0.25-arc-degree resolution. The unit of PBLH is meter (m).

In the model design stage, many other variables are considered, including humidity, nighttime light, wind speed, cloud pressure, aerosol optical depth, ultraviolet aerosol index, among others. However, none of these variables are included and prediction for either their poor improvement or the multicollinearity. For example, the correlation coefficient

between humidity and precipitation significantly exceeds 0.5. Furthermore, the correlation coefficient between humidity and temperature is over 0.7, while the relationship between precipitation is not so strong, only 0.15. Therefore, we keep the precipitation in the analysis. Moreover, the results of GWPR are spatial point data frames. To secure the coefficient rasters for the prediction, we have to use interpolation methods, which would apparently cause some slight errors. If the benefit from involving one more variable cannot offset the errors in its interpolation, it should not be taken into account. In view of numerous tests, finally, the TrCA NO<sub>2</sub>, terrain atmospheric pressure, temperature, NDVI, precipitation, and PBLH are selected as independent variables.

### *Descriptive Statistics*

The data from the abovementioned resources are cleaned to establish an unbalanced dataset for modeling and prediction with time stamps and geographical locations from January 2015 to October 2021. The number of complete observations in this data set is 29,686. The unbalance of data expresses in both temporal and spatial extent. Every city has at least five-month, and at most 65-month data, i.e., it is the imbalance in temporal extent. Moreover, the spatial distribution is also unbalanced. For instance, the smallest distance between the two closest cities is 0.103 arc degree, while the largest distance is 24.710 arc degrees. As shown in **Figure 1**, most cities with the data are located in Northern Hemisphere, while only a few of them distribute in South America and Africa, which drives increased difficulty of the interpolation. Statistical distributions and descriptive statistics of the variables are illustrated and summarized in **Figure 3**. The concentration of ground-level NO<sub>2</sub> has a mean value of 19.47  $\mu\text{g}/\text{m}^3$  and a standard deviation (SD) of 14.19

$\mu g/m^3$ . Its 1<sup>st</sup> quantile, median, 3<sup>rd</sup> quantile are  $10.56 \mu g/m^3$ ,  $16.59 \mu g/m^3$ , and  $24.81 \mu g/m^3$ , respectively. Its statistical distribution is one peak and right-skewed because the skewness is 7.17. The 1<sup>st</sup> quantile, median, 3<sup>rd</sup> quantile of the monthly TrCA NO<sub>2</sub> are  $1347.52 \mu g/m^2$ ,  $2139.54 \mu g/m^2$ , and  $3955.21 \mu g/m^2$ , with a mean value of  $3411.90 \mu g/m^2$  and an SD of  $3806.50 \mu g/m^2$ . Due to the 4.17 skewness, the statistical distribution of the monthly TrCA NO<sub>2</sub> is one right-skewed peak. The monthly terrain atmospheric pressure has a mean of 974.32 hPa, an SD of 60.43 hPa, a 1<sup>st</sup> quantile of 967.6 hPa, a median of 998.6 hPa, and a 3<sup>rd</sup> quantile of 1009.5 hPa. Its statistical distribution is one left-skewed peak, whose skewness is -2.37. The monthly average temperature has a mean of  $14.98 ^\circ C$  and an SD of  $10.33 ^\circ C$ , whose 1<sup>st</sup> quantile, median, 3<sup>rd</sup> quantile are  $7.36 ^\circ C$ ,  $16.17 ^\circ C$ , and  $22.99 ^\circ C$ . The shape of the distribution is one slightly left-skewed peak because of its skewness of -0.39. The NDVI has a mean value of 0.47, an SD of 0.17, a 1<sup>st</sup> quantile of 0.36, a median of 0.48, and a 3<sup>rd</sup> quantile of 0.60. The statistical distribution is one peak and slightly left-skewed (skewness: -0.34). The mean, SD, 1<sup>st</sup> quantile, median, and 3<sup>rd</sup> quantile of the precipitation are  $0.12 kg/(m^2 \cdot h)$ ,  $0.11 kg/(m^2 \cdot h)$ ,  $0.05 kg/(m^2 \cdot h)$ ,  $0.09 kg/(m^2 \cdot h)$ , and  $0.15 kg/(m^2 \cdot h)$ , respectively. The shape of its statistical distribution is one right-skewed peak because its skewness is 2.25. The mean, SD, 1<sup>st</sup> quantile, median, and 3<sup>rd</sup> quantile of the PBLH are 755.92m, 313.13m, 550.6m, 712.8m, and 896.4m, respectively. The statistical distribution of the PBLH is one right-skewed peak (skewness: 1.79).

*Figure 3 is located here.*

The linear trends and correlation coefficients between the concentration of ground-level NO<sub>2</sub> and other variables are examined, shown in **Figure 4**. In **Figure 4**,  $r$  and  $p$

266 represent Pearson's correlation coefficient and p-value, respectively (Taylor 1990). The  $r$   
 267 is calculated as follows:

$$r = \frac{\sum_{i=1}^n (X1_i - \bar{X1})(X2_i - \bar{X2})}{\sqrt{\sum_{i=1}^n (X1_i - \bar{X1})^2} \sqrt{\sum_{i=1}^n (X2_i - \bar{X2})^2}} \quad (3)$$

268 where  $r$  is the correlation coefficient,  $X1$  and  $X2$  are the aimed variables put into the test,  
 269 and  $n$  is the data size. To estimate the significance of the correlation coefficient, we  
 270 calculate the t-test value ( $t$ ), at first:

$$t = \frac{r\sqrt{n-2}}{\sqrt{1-r^2}} \quad (4)$$

271 Here, the p-value ( $p$ ) is calculated as follows:

$$p = 2 \times \Pr(T > t) \quad (5)$$

272 where  $T$  follows a t distribution with  $n - 2$  degrees of freedom, and  $\Pr(T > t)$  represents  
 273 the probability of  $T > t$ . According to **Figure 4**, all correlation coefficients are significant  
 274 at the 0.1 level. Albeit the coefficient of the correlation between ground-level NO<sub>2</sub>  
 275 concentration and terrain atmospheric pressure is only -0.02, we still consider that it affects  
 276 the ground-level NO<sub>2</sub> concentration as demonstrated by **Equation 2**.

277 *Figure 4 is located here.*

278

## 279 **Methodology**

### 280 *Spatially Stationary Global Model*

281 We first assume that the relationships between the ground-level concentration of  
 282 NO<sub>2</sub> and other independent variables are spatially stationary. That is to say, those  
 283 relationships do not vary by spatial contexts (Brunsdon et al. 1998; Fotheringham et al.

2002). We apply the three typical global models, random effects model (REM), fixed effects model (FEM), and POLS, to estimate the relationships among the variables. The only difference among these three global models is the time-fixed effects in the models. Therefore, substantial tests about the time-fixed effects are required.

The global model selection is executed. In order to compare FEM with POLS, the F test for individual effects is employed. FEM is better than POLS since the test result is significant, and the null hypothesis that no time-fixed effects are needed is rejected (Breusch and Pagan 1980; Croissant and Millo 2008). Based on the Breusch-Pagan Lagrange Multiplier test for random effects, the significant result indicates that REM is appropriate because the null hypothesis that no time-fixed effects are needed is not accepted, either (Breusch and Pagan 1980). We also run the Hausman test to detect the reasonable model between FEM and REM (Kang 1985). The significant result indicates FEM is preferred, as the null hypothesis that the preferred model is REM is rejected. Here, FEM in our analysis is illustrated as follows:

$$GNO2_{it} = \beta X'_{it} + \alpha_i + \mu_{it} \quad (6)$$

where  $GNO2_{it}$  denotes the monthly average ground-level concentration of  $NO_2$  ( $\mu g/m^3$ ) in measurement  $i$  during  $t$  month,  $X_{it}$  denotes a matrix of independent variables, including TrCA of  $NO_2$  ( $\mu g/m^2$ ), terrain atmospheric pressure (hPa), temperature ( $^{\circ}C$ ), NDVI, precipitation ( $kg/(m^2 \cdot h)$ ), PBLH (m), and year dummy variables in measurement  $i$  during  $t$  month,  $\alpha_i$  denotes the time-fixed effects,  $\mu_{it}$  denotes an idiosyncratic error, and  $\beta$  is a vector of parameters to be estimated. Some ignored variables, such as air pollution policy in countries, economic status, among others, are changed year by year. We, therefore, add the year dummy variables to the model.

306

307 *Spatially Non-stationary Local Model*

308         Unlike traditional linear regression models, like REM, FEM, and POLS, the  
309 geographically weighted panel regression (GWPR) allows the coefficients to vary spatially  
310 (Brunsdon et al. 2010; Fotheringham and Oshan 2016). Because the relationship between  
311 the dependent variable and the independent variables could vary by the spatial context, the  
312 estimation accuracy of ground-level NO<sub>2</sub> concentration, such as R<sup>2</sup> of models, dramatically  
313 improves. Basically, the GWPR divides the total sample into numerous sub-samples,  
314 according to the optimal bandwidth and spatially weighted matrix. The bandwidth in  
315 GWPR is the threshold distance to judge whether two objects have a spatial relationship  
316 (Beenstock and Felsenstein 2019; Brunsdon et al. 2010; Brunsdon et al. 1998). If two  
317 objects have a spatial relationship, they are considered as the neighbors of each other.  
318 Currently, two types of bandwidth are widely used, fixed distance bandwidth and adaptive  
319 distance bandwidth (Gollini et al. 2015). Literally, the fixed distance bandwidth is a fixed  
320 threshold distance, and if two spatial objects are within this distance, they are spatially  
321 related. The adaptive distance bandwidth is an integer of the number of objects in a  
322 subsample because every object always has a certain number of neighbors. Hence, the  
323 threshold distance for each object might be different. To calibrate the optimal bandwidth  
324 in the GWPR, the mean square prediction error is the critical index. When the mean square  
325 prediction error is the smallest, the model with a certain bandwidth has the highest accuracy  
326 (Gollini et al. 2015). Taking a specific bandwidth ( $b$ ), the mean square prediction error is  
327 calculated as follows:

$$MSPE(b) = \frac{m \sum_j [y_j - \widehat{y_j(b)}]^2}{(m - p + 1)^2} \quad (7)$$

where  $MSPE(b)$  is the mean square prediction error based on a specific bandwidth  $b$ ,  $m$  is the data size,  $y_j$  is the dependent variable's value of the  $j$ th record,  $\widehat{y_j(b)}$  is the predicted value of the  $j$ th record based on the bandwidth  $b$ , and  $p$  is the number of the parameters in the analysis. It must be noted that the bandwidth  $b$  can be either the fixed distance bandwidth or the adaptive distance bandwidth here. The GWPR is an improvement of geographically weighted regression (GWR). In the GWR, previous studies generally assume that **Equation 7** is a U-shape function (Brunsdon et al. 1998; Fotheringham et al. 2002; Gollini et al. 2015). However, as those studies mentioned, there is no statistical or mathematical evidence for or against this assumption. The benefit from this assumption is the reduction of calculating time because the calculation could use the golden-section search to find the extremum to obtain optimal bandwidth (Gollini et al. 2015).

The step increment selection is applied to calibrate the optimal bandwidth due to the recently designed program, which requires fewer computer resources. We calibrate the optimal fixed and adaptive distance bandwidths. In the fixed distance bandwidth selection, the selection extent is from 0.25 arc degree to 20 arc degrees, and the examined bandwidth increases 0.25 arc degree every time because the spatial resolution of all the grid data is 0.25 arc degree. The optimal fixed distance bandwidth is 2.25 arc degrees, as shown in **Figure 5**. Since the spatial distribution of the cities with data is unbalanced and some points are far from others (**Figure 2**), many points would have no neighbor if using this bandwidth. Data islands severely destroy the stability of the GWPR because they have no relationship with other points in the data set. Both dropping the data islands and increasing the bandwidth would slash the accuracy of the analysis. Hence, we adopt the adaptive distance



bandwidth. In the adaptive distance bandwidth selection, the selection extent is from 4 to 100, and the tested bandwidth increases one every time. When the adaptive distance bandwidth is less than 4, some local regressions do not have enough degrees of freedom. According to the analysis, the optimal adaptive distance bandwidth is selected, which is 7. In other words, in each subsample, there are seven cities' data involved in locally weighted regression.

*Figure 5 is located here.*

Spatially weighted matrix, based on the calibrated bandwidth, is calculated as follows:

$$\mathbf{w}_i = \begin{cases} [1 - (\frac{\mathbf{d}}{b_i})^2]^2, & \text{if } d_k \leq b_i \\ 0, & \text{if } d_k > b_i \end{cases} \quad (8)$$

where  $\mathbf{w}_i$  denotes a vector of spatial weights between city  $i$  and its neighbors,  $\mathbf{d}$  represents a vector of distances between city  $i$  and its neighbors,  $b_i$  is the threshold distance of city  $i$ 's neighbors, and  $d_k$  is the distance between city  $i$  and city  $k$ . It should be emphasized that  $b_i$  might vary city by city, as here we use the adaptive distance bandwidth. Every vector is a column of the spatially weighted matrix. According to the spatial weights vectors, the total sample is divided into 529 sub-samples, taking every city as the center, respectively.

The GWPR estimates the coefficients in every location in light of the spatially weighted matrix. In global models statistical tests, FEM is the preferred model, and in the locally statistically test, most local regressions show significant time-fixed effects. Therefore, the GWPR model is also following FEM. The GWPR model is expressed as follows:

$$GNO2_{it} = \beta_i X'_{it} + \alpha_i + \epsilon_{it} \quad (9)$$

370 where  $\beta_i$  denotes a vector of parameters in the regression with the sub-sample taking the  
 371 city  $i$  as the center. In term of the equation expression, the only difference between FEM  
 372 (**Equation 6**) and the GWPR based on FEM (**Equation 9**) is that  $\beta_i$  varies spatially. It  
 373 must be noted that the algorithm would change to the GWPR based on POLS, if we directly  
 374 use GWR method. According to cross validation, the accuracy and stability of the GWPR  
 375 based on POLS is lower than the GWPR based on FEM. In this way, the new method,  
 376 GWPR, is necessary for this analysis.

377 To estimate the coefficient in the GWPR, because the time-fixed effects ( $\alpha_i$ ) is  
 378 unknown (Croissant and Millo 2008), we need to expand **Equation 9**, as follows.

381

$$GNO2_{it} - \hat{\theta}_i \overline{GNO2}_i = (1 - \hat{\theta}_i) \beta_{0i} + \beta_i (X_{it} - \hat{\theta}_i \overline{X}_i)' + (\epsilon_{it} - \hat{\theta}_i \overline{\epsilon}_i) \quad (10)$$

382 where  $\hat{\theta}_i$  denotes the share of the individual effects in the total effects,  $\overline{GNO2}_i$  denotes the  
 383 mean of the ground-level NO2 concentration in the data set in the city  $i$ ,  $\beta_{0i}$  is the estimated  
 384 intercept in the city  $i$ ,  $\overline{X}_i$  denotes a vector of means of independent variables in the city  $i$ ,  
 385 and  $\overline{\epsilon}_i$  denotes the mean of the error in the city  $i$ . If the GWPR follows the data  
 386 transformation of FEM, the  $\hat{\theta}_i$  is always equal to 1. So  $\beta_{0i}$  is removed, in the GWPR based  
 387 on FEM. To simplify Equation (10), we define the matrix of independent variables  $x_{it}$  and  
 388 the dependent variable  $gno2_{it}$  as follows:

$$x_{it} = X_{it} - \overline{X}_i \quad (11)$$

$$gno2_{it} = GNO2_{it} - \overline{GNO2}_i \quad (12)$$

$$\sigma_{it} = \epsilon_{it} - \overline{\epsilon}_i \quad (13)$$

389 In the light of **Equation 10-13**, the GWPR model is transformed as follows:

$$gno2_{it} = \beta_i \mathbf{x}'_{it} + \sigma_{it} \quad (14)$$

390 This algorithm becomes the typical GWR without the intercept. The coefficient estimation  
391 could be displayed as follows:

$$\beta_i = [\mathbf{x}_{it}^T \mathbf{W}_i \mathbf{x}_{it}]^{-1} \mathbf{x}_{it}^T \mathbf{W}_i gno2_{it} \quad (15)$$

392

### 393 *Statistical Indicators*

394 Several statistical indicators, including  $R^2$ , root mean square error (RMSE), mean  
395 absolute error (MAE),  $r$  between observed and predicted values, and regression coefficients  
396 between observed and predicted values, are widely used in previous studies (Kim et al.  
397 2021; Li and Wu 2021; Liu et al. 2017) and also applied to evaluate the estimation accuracy  
398 of the GWPR model.  $R^2$  is a critical statistical indicator describing the goodness of fit. The  
399 high  $R^2$  in the models means that the discrepancy between predicted  $\text{NO}_2$  concentration  
400 and measured ground-level  $\text{NO}_2$  concentration is tiny. The  $R^2$  calculation algorithm is  
401 shown as follows:

$$R^2 = 1 - \frac{\sum_{k=1}^n (MNO2_k - PNO2_k)^2}{\sum_{k=1}^n (MNO2_k - \overline{MNO2})^2} \quad (16)$$

402 where  $n$  represents the observation number in the total sample,  $MNO2_k$  represents the  $k$ th  
403 record of the measured ground-level  $\text{NO}_2$  concentration,  $PNO2_k$  represents the  $k$ th record  
404 of the predicted  $\text{NO}_2$  concentration, and  $\overline{MNO2}$  represents the mean of the measured  
405 ground-level  $\text{NO}_2$  concentration. It must be noted that this  $R^2$  of the GWR or the GPWR is  
406 the global value because here the total sample is used. The RMSE is also calculated,  
407 indicating the differences between predicted  $\text{NO}_2$  concentration and measured ground-

level NO<sub>2</sub> concentration. The RMSE is sensitive to both systematic error and random error, shown as follows:

$$RMSE = \sqrt{\frac{1}{n} \sum_{k=1}^n (MNO2_k - PNO2_k)^2} \quad (17)$$

The MAE is calculated as follows:

$$MAE = \text{mean}(|MNO2_k - PNO2_k|) \quad (18)$$

In the analysis, the MAE should be low. Additionally, the regression coefficients between observed and predicted values are imputed as follows:

$$MNO2_k = \alpha + \beta PNO2_k + \delta_k \quad (19)$$

where  $\alpha$  is the intercept in the regression and the ideal value of  $\alpha$  is 0,  $\beta$  is the slope and it ideal value is 1, and  $\delta_k$  is a random error term.

#### Spatial Interpolation of the Coefficients

We use the ordinary Kriging (OK) method to interpolate the coefficients of the GWPR result into rasters. Directly using the GWPR result is insufficient to predict and obtain the ground-level NO<sub>2</sub> concentration raster data because the result is a spatial point data frame and the coefficients spatially vary. In the beginning, the inverse distance weighting (IDW) and OK method are considered. To choose the reasonable interpolation method, these two methods are examined by leave-one-out cross validation. The result shows that the OK method is more stable than IDW, consistent with the previous study (Li and Heap 2011). The general form of the OK method is expressed (Pebesma 2004) as follows:

$$\hat{\beta}(s_0) = \sum_{l=1}^m \lambda_l \beta(s_l) \text{ with } \sum_{l=1}^m \lambda_l = 1 \quad (20)$$

where  $\hat{\beta}(s_0)$  represents the coefficient at unobserved location  $s_0$ ,  $\beta(s_l)$  represent the coefficient value at known location  $s_l$ ,  $\lambda_l$  is the spatial weight for the coefficient value at the  $l$ th location, and  $m$  is the number of known values. To obtain optimal  $\lambda_l$ , there are two requirements in OK: unbiased and minimal variance of estimation. If  $\sum_{l=1}^m \lambda_l$  is equal to 1, then it is unbiased (Pebesma 2004). To minimize the estimation variance, we use the spherical semi-variance mathematical model. Harnessing the OK method, the GWPR results would be estimated to several coefficient rasters with a 0.25-arc-degree spatial resolution. Additionally, the mean value rasters of variables are also interpolated by the OK method. In the prediction process, the data transformations following **Equations 11** and **12** are necessary. To check the reliability of the interpolation process, the leave-one-out cross validation is applied. Simply, the leave-one-out cross-validation requires the number of folds equals the numbers of cities in our data set. In the cross validation process, one certain city is selected as the test set, while all other 529 cities are used as the training set. This process will happen 530 times until all the cities have been selected as the test set.

#### *Predictions of Ground-level NO<sub>2</sub> Concentration and Change Trends*

The monthly global ground-level NO<sub>2</sub> concentration raster data are predicted based on the original raster data, coefficient rasters, and mean value rasters, following **Equation 14**. Furthermore, because the ground-level NO<sub>2</sub> concentration cannot be minus, any value less than zero is set to zero in the prediction grid data. There are 82-month grid data obtained from the prediction process. To detect the monthly change trends of each grid, the monthly NO<sub>2</sub> concentrations of each grid are regressed with their month order. The first

month of our data set is January 2015, so the month order of data in January 2015 is the 1<sup>st</sup>. Lastly, the month order of October 2021 is the 82<sup>nd</sup>. The monthly change trends are estimated as follows:

$$PNO2_{LT} = \alpha_L + \beta_L MO_T + \varphi_{LT} \quad (20)$$

where  $PNO2_{LT}$  is the predicted NO<sub>2</sub> concentration in the grid  $L$  in the  $T$ th month,  $MO_T$  is the month order of  $PNO2_{LT}$ ,  $\alpha_L$  is the intercept in the grid  $L$ ,  $\beta_L$  is the monthly NO<sub>2</sub> concentration change trend in the grid  $L$ , and  $\varphi_{LT}$  is a random error term. It must be noted that the data from a certain grid should be performed the regression once if there are no less than 30 records. Additionally, every individual regression just uses the data from one grid.

## Results

### *Validation of the GWPR Result*

The overall accuracy of the GWPR based on FEM is 74.45%, the RMSE is 7.171  $\mu g/m^3$ , and the is MAE 3.48  $\mu g/m^3$ . **Figure 6** shows the relationship between predicted and measured ground-level NO<sub>2</sub> concentrations in the GWPR. The coefficient of the correlation ( $r$ ) between predicted and measured values are 0.8632, following **Equation 3**, that is, there is a strong correlation. Furthermore, the OLS regression between measured and predicted values also illustrates the significant relationship since the slope is roughly 1.021 significantly, and the ideal value is 1. To confirm whether the goodness of fit of a specific year is apparently lower than other years', we calculate all the yearly statistical indicators. In **Table 1**, the yearly statistical indicators, including  $R^2$ , RMSE, correlation

coefficient ( $r$ ), the slope and intercept of regressions between measured and predicted values, are listed. The lowest yearly  $R^2$  is 51.54% in 2021. The yearly RMSE and MAE peak in 2021 and 2018, respectively, which is 9.619 and 4.071  $\mu\text{g}/\text{m}^3$ . Comparisons of monthly time series illustrate that the GWPR captures the monthly temporal variability accurately (**Figure 7**).

*Figure 6 is located here.*

*Table 1 is located here.*

*Figure 7 is located here.*

**Table 2** reports the results of 10-fold cross validation. The total data set is randomly divided into ten subsets. In every single cross validation, nine subsets are used to train the model. Then the reserved subset and the coefficients from the trained model are employed to predict the dependent variable. The performance of the GWPR based on FEM is stable in terms of goodness of prediction for the test subsets. The lowest accuracy of prediction for the test subset is 68.55%, and its RMSE, MEA, and coefficient ( $r$ ) of the correlation between predicted and measured values are 15.569  $\mu\text{g}/\text{m}^3$ , 4.399  $\mu\text{g}/\text{m}^3$ , and 0.627, respectively. According to the 10-fold cross validation results, the reliability of the GWPR model is shown.

*Table 2 is located here.*

### ***Validation of the OK Interpolations***

**Table 3** illustrates the result of leave-one-out cross validation of the coefficient and mean value interpolations (Pebesma 2004). The worst performance of the OK method is

from the interpolation of the mean value of measured ground-level NO<sub>2</sub>, whose R<sup>2</sup> is 34.50%, but its RMSE and MAE are not high, which are 7.773 and 5.633  $\mu\text{g}/\text{m}^3$ , respectively. For the low values of its RMSE and MAE, this interpolated grid data set is still acceptable. There is a new indicator named on point R<sup>2</sup> in **Table 3**. This indicator is to depict how much the observed values change after interpolation. In the OK method, the spatial weight might not equal 1 when the distance between two points equals 0, i.e., they are overlapped. Hence, after OK interpolation, the predicted values from the imputed grid data set might differ slightly from the observed values. The on-point R<sup>2</sup> indicates that none of the interpolations lose the accuracy more than 2%, and most of them only slash 0.1% accuracy.

*Table 3 is located here.*

### ***Prediction and Monthly Change Trends***

The accuracy of the predicted grid data set is 69.61%, and the RMSE and MAE are 7.82 and 4.07  $\mu\text{g}/\text{m}^3$ , respectively. Due to the slight change in the interpolation process, the accuracy in the final prediction is lower than the result of GWPR. **Figure 8** demonstrates the relationship between predicted and measured ground-level NO<sub>2</sub> concentrations in the predicted grid data sets. The  $r$  is 0.8376, lower than the  $r$  in the GWPR result (0.8585). According to the tiny difference of all statistical indicators between the GWPR result and the grid data prediction result, the final prediction data are reasonable.



Figure 8 is located here.

**Figure 9** presents the average monthly ground-level NO<sub>2</sub> concentration. The result shows that ground-level NO<sub>2</sub> concentration in Asia is relatively higher than in other continents. Moreover, in western Asia, the ground-level NO<sub>2</sub> pollution is most severe. In most regions of Iran, Iraq, and Turkmenistan, the average values even exceed 100  $\mu\text{g}/\text{m}^3$ , much higher than WHO's ambient NO<sub>2</sub> concentration limits, which is an annual mean of 40  $\mu\text{g}/\text{m}^3$  in link with previous studies (Kasparoglu et al. 2018; Yousefian et al. 2020). Moreover, partial regions in northern China, India, Chile, Bolivia, South Africa, northern Italy, and the west coast of the United States are also severely polluted, tallying with previous research (Di et al. 2020; Kim et al. 2021; Zheng et al. 2019). **Figure 10** shows the average monthly TrCA NO<sub>2</sub> concentration. The spatial distribution of severely polluted regions lines up with our predictions, which partially backs up our research. The monthly change trends of each grid are estimated following **Equation 20**. **Figure 11** illustrates the monthly change trends of each grid. All the values shown in **Figure 11** should be significant at the 0.1 level. Based on **Figure 11**, the ground-level NO<sub>2</sub> concentration is gradually decreasing in most regions in this world. However, in the Red Sea region, Arabian Peninsula, Persian Gulf, the ground-level NO<sub>2</sub> concentration is increasing, even though there are already the most severely polluted areas. In addition, the changes in most places of India and Mexico also show an upward trend. In some areas of California and Nevada, the United States, the change trends are on the rise.

Figure 9 is located here.

Figure 10 is located here.

Figure 11 is located here.

## Discussion

The GWPR model is employed to examine the association of satellite-derived data with measured ground-level NO<sub>2</sub> concentrations from January 2015 to October 2017, among 530 cities. The accuracy of our new version of GWPR (74.45%) exceeds the previous studies about regional ground-level NO<sub>2</sub> concentration (Kim et al. 2021; Li et al. 2020; Qin et al. 2017). Our analysis provides the first example of the GWPR on an unbalanced panel data set. There are 82 monthly global ground-level NO<sub>2</sub> concentrations with 0.25-arc-degree spatial resolution predicted from January 2015 to October 2021 (Shown in the **Supplementary Materials**). The monthly change trends of each grid are demonstrated in our analysis.

In terms of accuracy, our study is better than much other recent research on the ground-level NO<sub>2</sub> concentration estimation based on the satellite data set. The accuracy of a study on ground-level NO<sub>2</sub> concentration over Central-Eastern China employing geographically and temporally weighted regression is 0.60, lower than our 0.70 (Qin et al. 2017). Additionally, its MEA is 9.28  $\mu\text{g}/\text{m}^3$ , while our MEA is 5.633  $\mu\text{g}/\text{m}^3$ . A research over the Wuhan urban agglomeration applying space-time neural networks obtains 0.69 accuracy and an 8.29- $\mu\text{g}/\text{m}^3$  RMSE, while our RMSE is 7.82  $\mu\text{g}/\text{m}^3$  (Li et al. 2020). Additionally, a study over Switzerland and northern Italy using machine learning

technology provides a 59%-accuracy prediction, and its MEA is  $7.69 \mu\text{g}/\text{m}^3$  (Kim et al. 2021). However, these studies excel at either spatial or temporal resolution.

The spatial distribution and concentrations of the predictions is compared with previous studies. According to a study by Di et al., in the metropolitan areas of Michigan, Wisconsin, New England, Colorado, Nevada and California, the  $\text{NO}_2$  pollution is harmful, higher than 25 PPB (Di et al. 2020). Our prediction is in line with this study since the ground-level  $\text{NO}_2$  in those places is predicted around  $40 \mu\text{g}/\text{m}^3$  (Under an ambient pressure of 1 atmosphere and a temperature of  $25^\circ\text{C}$ , 1 PPB  $\text{NO}_2$  roughly equals  $1.88 \mu\text{g}/\text{m}^3$ ). Kasparoglu et al. put forward that in urban sites of Marmara regression of Turkey, the  $\text{NO}_2$  concentration are higher than  $75 \mu\text{g}/\text{m}^3$  (Kasparoglu et al. 2018), consistent with our study. Yousefian et al. propose that during 2012 - 2017, the  $\text{NO}_2$  concentration in Tehran, the Capital of Iran, is always 1.5 - 2.5 times higher than WHO limits ( $40 \mu\text{g}/\text{m}^3$ ) (Yousefian et al. 2020), where is also the most polluted area in our research. Kim et al.'s research hints that in an Alpine domain, the  $\text{NO}_2$  in the urban regions is always over  $40 \mu\text{g}/\text{m}^3$  (Kim et al. 2021), which is in keeping with our study. Additionally, Chi et al. estimate the annual average ground-level  $\text{NO}_2$  concentration in the main regions of China over 2014 – 2020 (Chi et al. 2021). Its results are similar to our predictions. To summarize, our study is in line with the most recent studies on ground-level  $\text{NO}_2$  concentration.

Our monthly grid data demonstrate that the temporal variation of the spatial distribution of the ground-level  $\text{NO}_2$  concentration is evident (Shown in Supplementary Materials and **Figure 7**). In December, January, and February, the  $\text{NO}_2$  pollution over the Northern Hemisphere is relatively serious, while it is high in June, July, and August over the Southern Hemisphere. The possible reasons for this temporal variation are as follows:

first, NO<sub>2</sub> can last longer or it is difficult to be removed in the low-temperature environment (Yousefian et al. 2020); second, residential energy for heating may produce more NO<sub>2</sub> (Fan et al. 2020); and third, the low temperature changes other meteorological factors eventually leading to NO<sub>2</sub> unable to spread to other zones far from the surface (Fan et al. 2020; Shen et al. 2021). However, no matter which is the main reason, the policymakers should take this temporal variation into account in the air pollution policies.

However, some limitations remain in our study. First, the measurement points are still limited, and their spatial distribution is unbalanced. In our dataset, there are only 530 cities taken into account globally without completely rural areas. Especially in Africa and South America, there are few measurement points. Secondly, the spatial resolutions of one control variable, namely PBLH, are not good enough. Thirdly, some hidden variables are ignored. For instance, the impacts of air pollution policies and COVID-19 are not involved in the research, though we have used year dummy variables to reduce their effects. Fourthly, the spatial and temporal resolutions are relatively low. Future studies are better to focus on the following topics. First, the relationship between ground-level NO<sub>2</sub> concentration and other satellite-derived data, such as aerosol optical depth and land cover, is needed to investigate. Secondly, the GWPR model should be further optimized. For example, if the data set contains data islands based on a certain bandwidth, whether the GWRP is still statistically reliable remains unknown. Thirdly, more confounders, such as land cover, human activity, among others, are needed in future analyses. Finally, the vertical distribution of NO<sub>2</sub> in air and its physical and chemical reasons are better to be carefully explored.

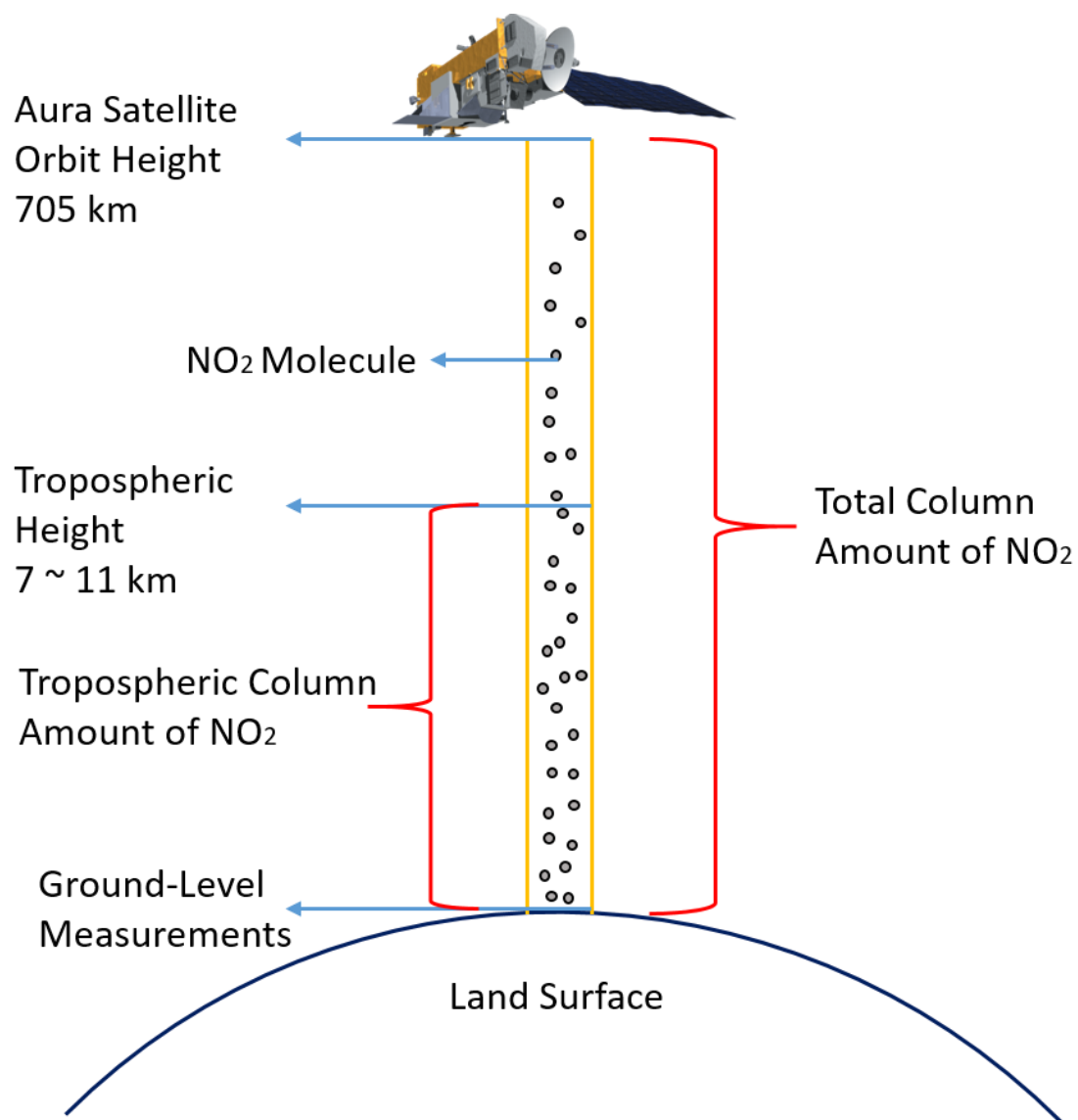
## Conclusions

In this study, a GWPR model is created to detect the spatial variation of the relationship between the measured ground-level NO<sub>2</sub> concentration and satellite-derived data and predict the monthly ground-level NO<sub>2</sub> concentration based on the data from the OMI and other satellite platforms. The GWPR model illustrates the outstanding R<sup>2</sup> (0.7445), *r* value (0.863), RMSE (7.171  $\mu\text{g}/\text{m}^3$ ) and MAE (3.480  $\mu\text{g}/\text{m}^3$ ) in the estimation and stability in the cross-validation. The GWPR is a simple but effective model to estimate monthly global ground-level NO<sub>2</sub> concentration at a 0.25-degree spatial resolution. The predictions provide critical basic data to environmental and public health science and valuable information for governments and societies to formulate more reasonable and efficient policies.

## Data Availability

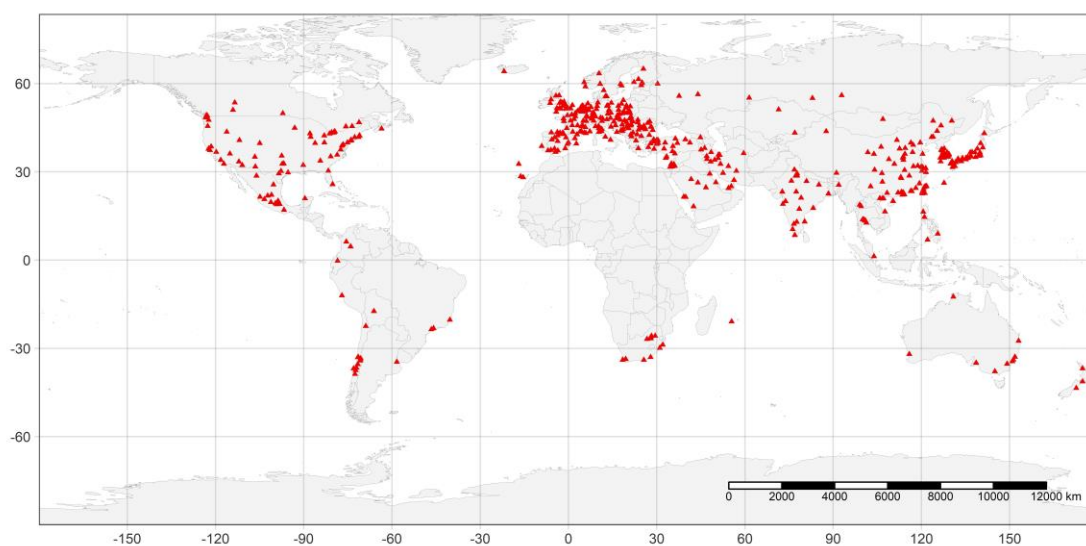
All data sources used in the analyses, along with fully reproducible code, are publicly available at [https://github.com/MichaelChaoLi-cpu/Monthly\\_Global\\_Ground\\_Level\\_NO2](https://github.com/MichaelChaoLi-cpu/Monthly_Global_Ground_Level_NO2).

616 **Figure**



617

618 **Figure 1: Illustration regarding TrCA, ToCA, and Ground-Level Measurements**



619

620

**Figure 2: Locations of Cities with the Measurement Points**

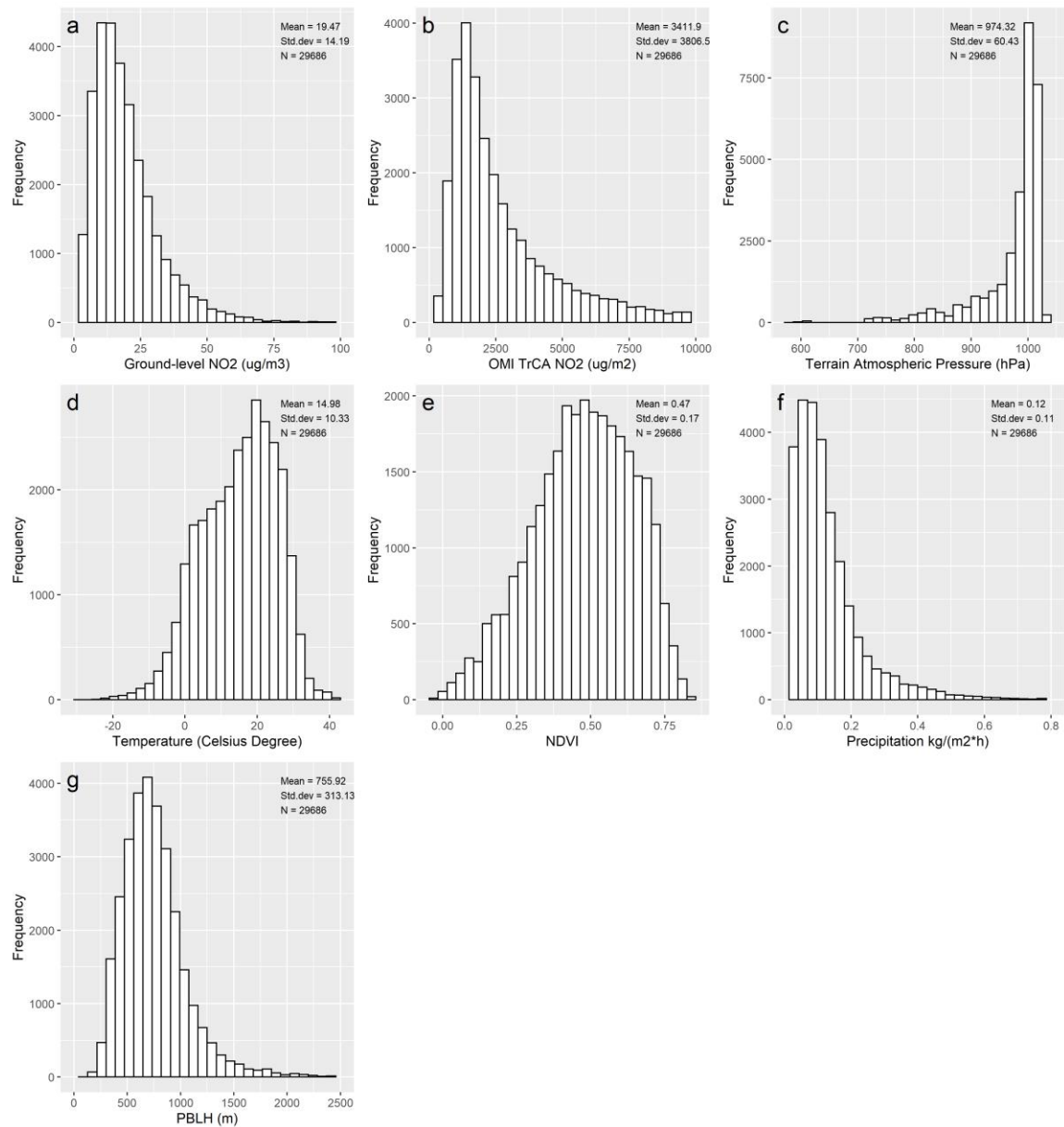


**Figure 3: Statistical Distributions and Descriptive Statistics of the Variables**



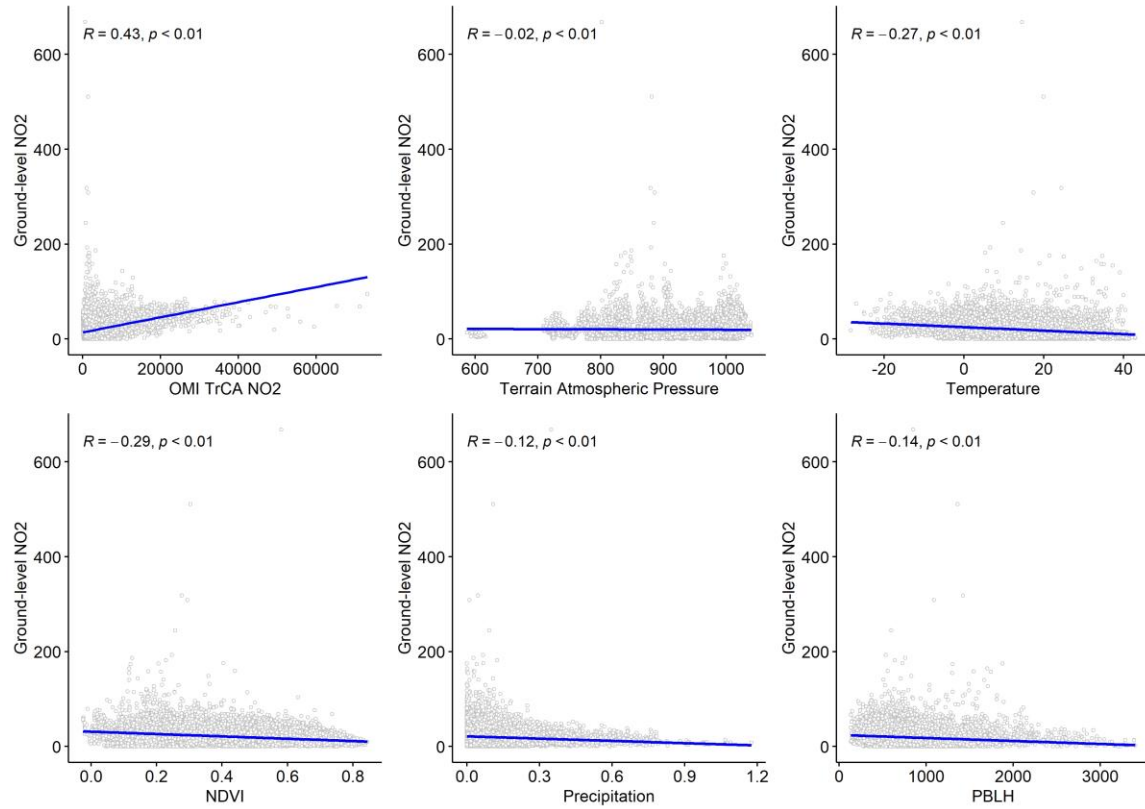


**Figure 4: Linear Trends and Correlation Coefficients**

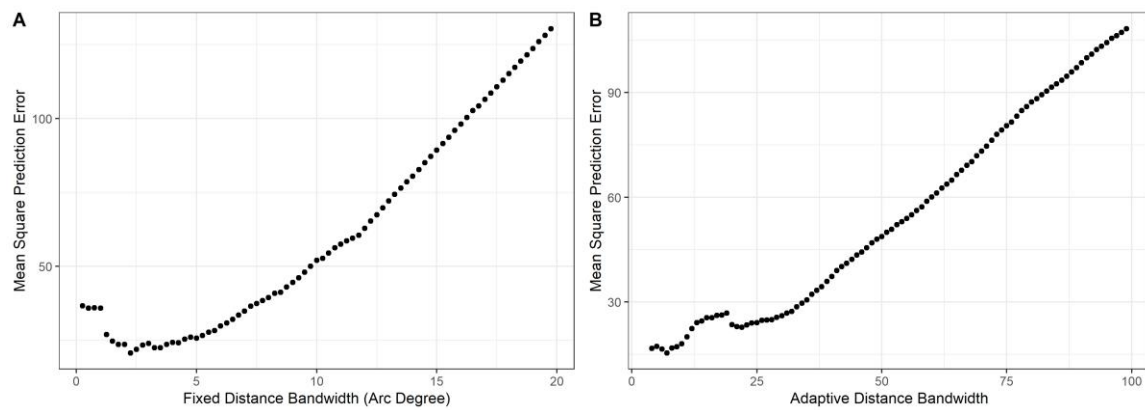


**Figure 5: Step Increment Bandwidth Selection**

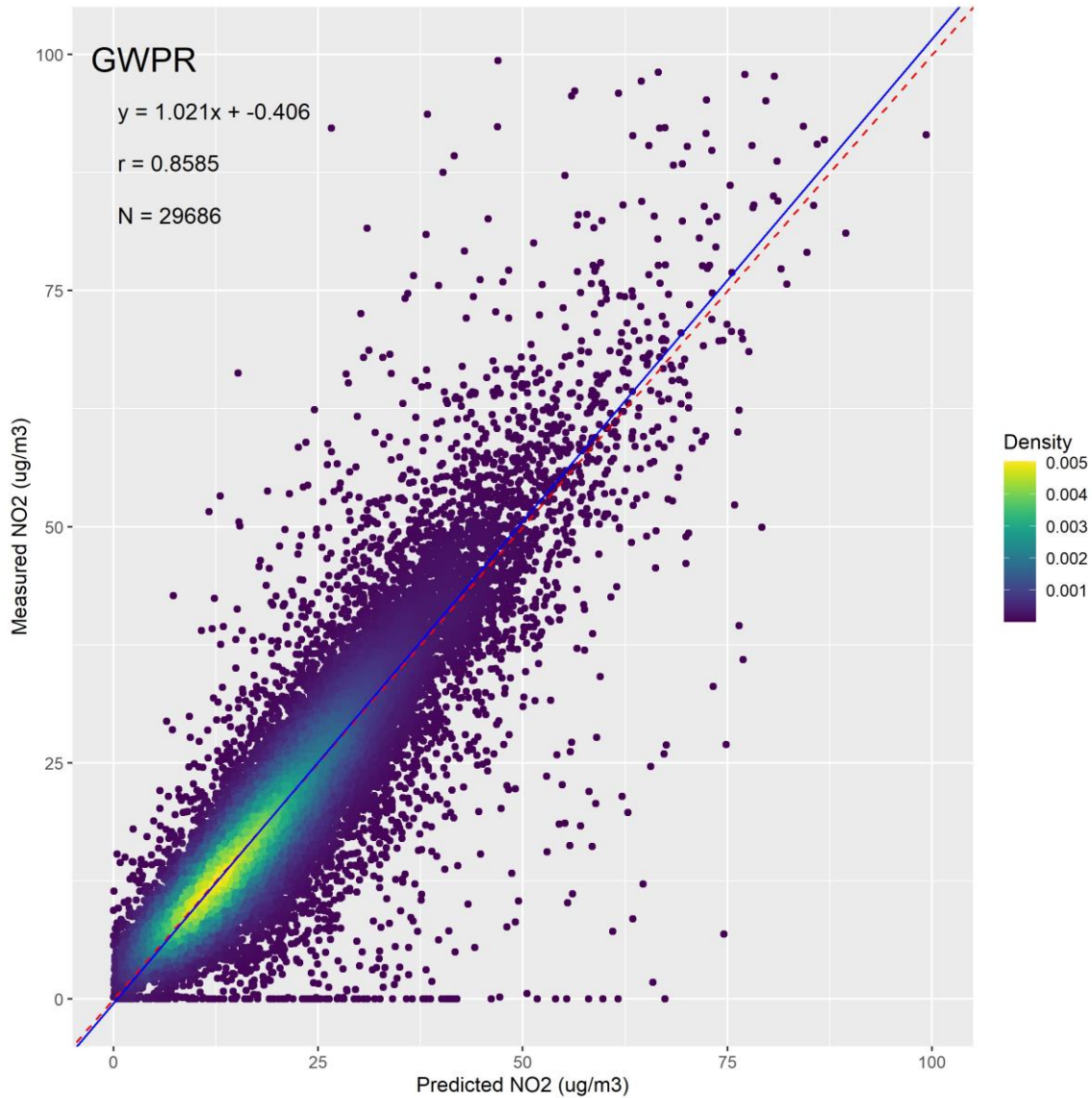


**Figure 6: The Density Plots between the Measured Ground-Level NO<sub>2</sub> Concentration and the Predicted NO<sub>2</sub> Concentration from the GWPR Result.**

(The red dashed line is the 1:1 line. The blue line is the regression line.)

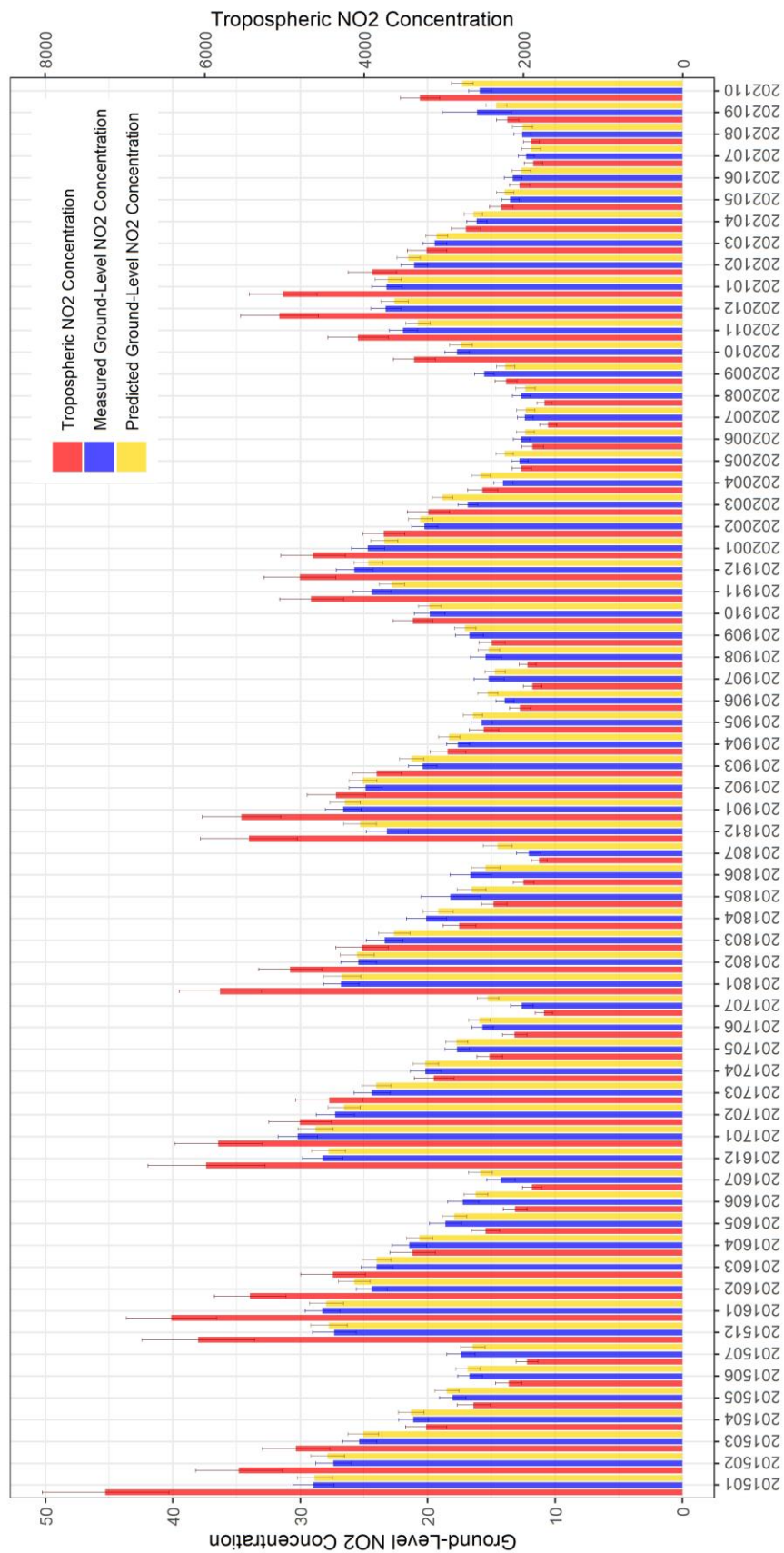
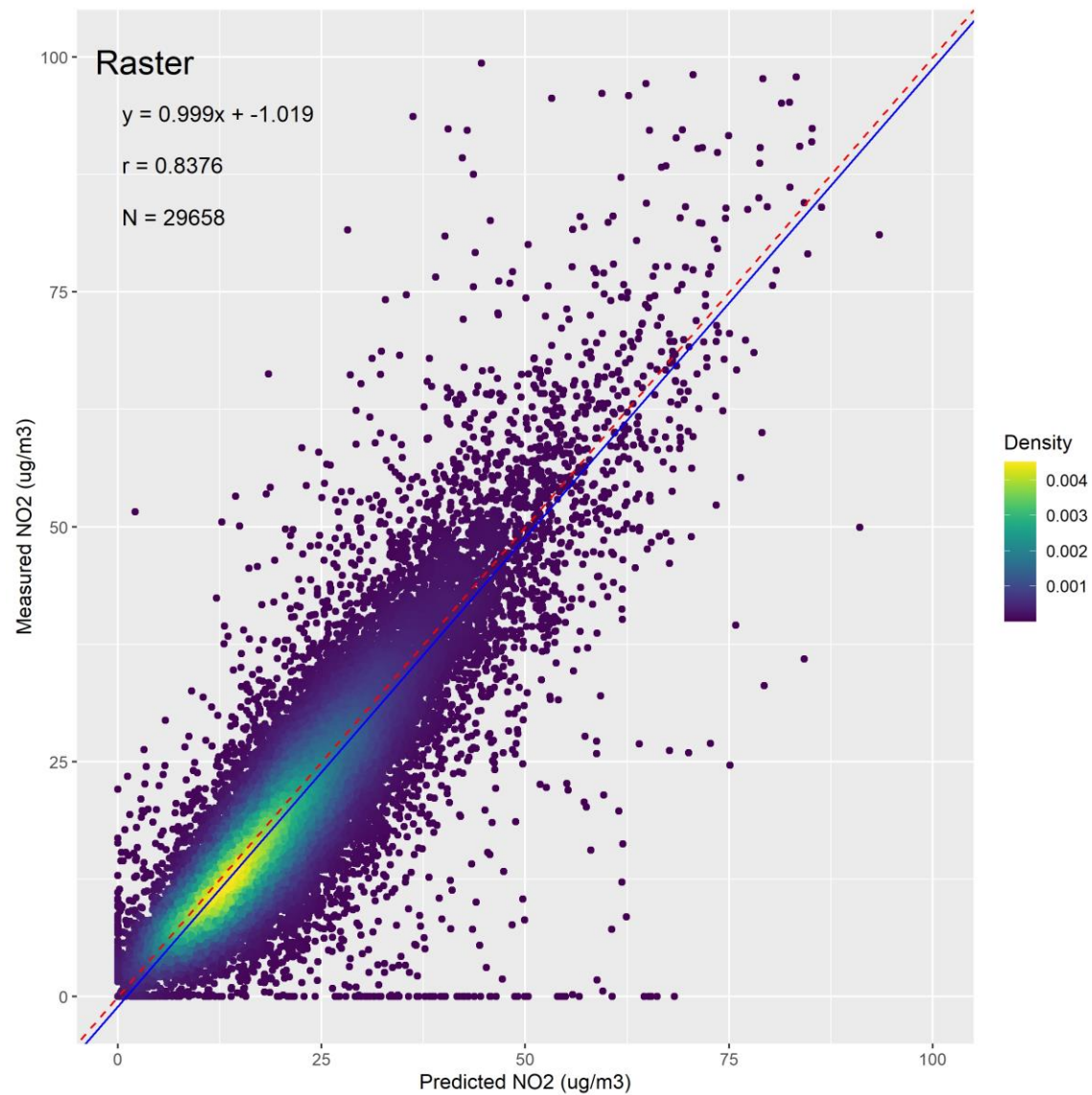


**Figure 7: Time Series Comparisons of Monthly Means of Tropospheric, Measured  
Ground-Level, Predicted Ground-Level NO<sub>2</sub> Concentration and Their 95%  
Confidence Interval**

(Unit: Tropospheric NO<sub>2</sub> Concentration [ $\mu\text{g}/\text{m}^2$ ], Measured and Predicted Ground-  
Level NO<sub>2</sub> Concentration [ $\mu\text{g}/\text{m}^3$ ])

640



641

642 **Figure 8: The Density Plots between the Measured Ground-Level NO<sub>2</sub>**  
643 **Concentration and the Predicted NO<sub>2</sub> Concentration from the Predicted Grid Data**  
644 **Sets.**

645 (The red dashed line is the 1:1 line. The blue line is the regression line.)

646

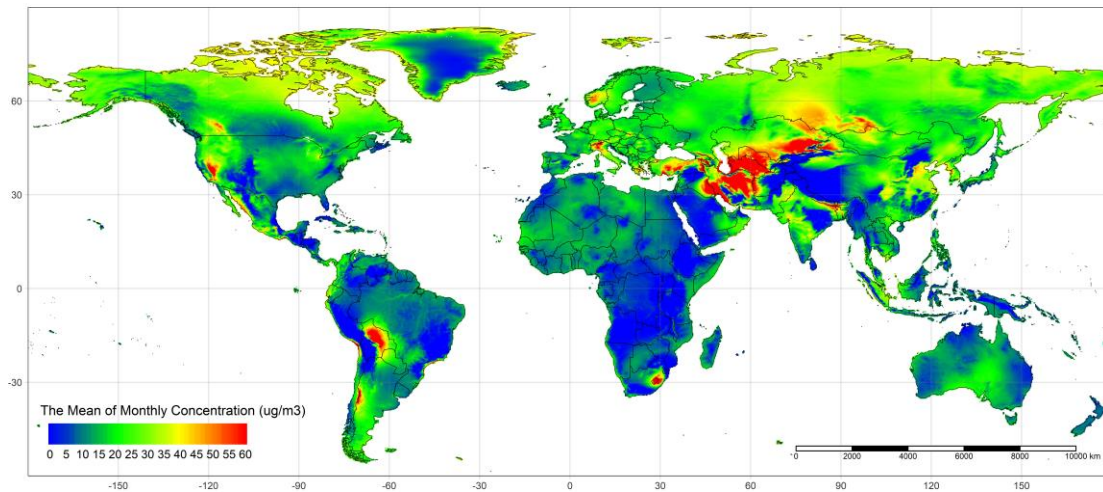


**Figure 9: Average Monthly Ground-Level NO<sub>2</sub> Concentration, Jan 2015 – Oct 2021**

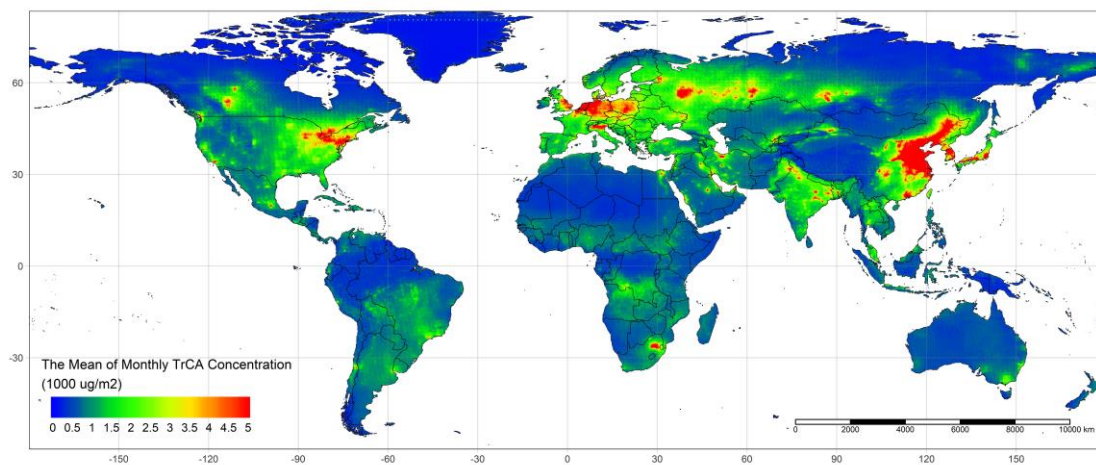


**Figure 10: Average Monthly TrCA NO<sub>2</sub> Concentration, Jan 2015 – Oct 2021**



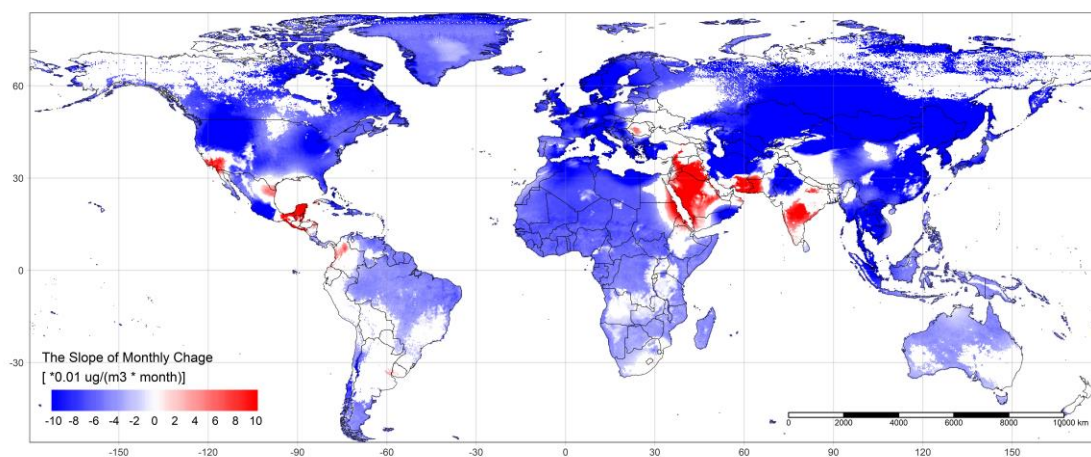


**Figure 11: Monthly Change Trends of Ground-Level NO<sub>2</sub> Concentration, Jan 2015  
– Oct 2021**

**Table 1: Yearly Statistical Indicators Summary of the GWPR Results**

Year	N	R <sup>2</sup>	RMSE	MAE	r	Slope	Intercept
2015	3115	86.46%	5.151	3.476	0.930	0.843	3.623
2016	3315	81.64%	6.126	3.617	0.904	0.794	4.508
2017	2936	85.20%	5.442	3.355	0.925	0.803	4.242
2018	3560	74.99%	8.881	4.071	0.869	0.689	6.461
2019	5790	71.34%	7.475	3.566	0.846	0.676	6.418
2020	6023	77.32%	5.317	3.335	0.881	0.827	2.912
2021	4947	51.55%	9.619	3.115	0.718	0.520	7.831
Total	29686	74.45%	7.171	3.480	0.863	0.724	5.373

Note: The Ideal value of slope is 1, and the ideal value of intercept is 0.

658

**Table 2: Statistical Indicators Summary of 10-Fold Cross Validation**

Statistical Indicator of Training								Statistical Indicator of Testing						
	N	R2	RMSE	MAE	r	Slope	Intercep t	N	R2	RMSE	MEA	r	Slope	Intercep t
1	26718	89.68%	7.746	3.800	0.839	0.681	6.195	2968	89.73%	7.669	4.096	0.831	0.691	6.139
2	26718	89.47%	7.843	3.861	0.837	0.684	6.151	2968	89.90%	7.422	4.367	0.825	0.733	5.296
3	26718	89.54%	7.828	3.846	0.839	0.683	6.148	2968	91.42%	6.754	3.994	0.844	0.799	4.160
4	26718	92.53%	6.464	3.719	0.876	0.749	4.926	2968	68.55%	15.57	4.399	0.627	0.358	12.275
5	26718	89.96%	7.640	3.763	0.844	0.692	6.009	2968	91.02%	7.155	4.055	0.854	0.711	5.592
6	26718	90.04%	7.637	3.828	0.847	0.694	5.960	2968	90.13%	7.267	4.025	0.826	0.793	4.044
7	26718	89.61%	7.777	3.790	0.839	0.681	6.226	2968	92.39%	6.546	3.997	0.875	0.762	4.511
8	26718	90.55%	7.404	3.724	0.853	0.705	5.756	2968	89.39%	7.875	4.171	0.834	0.683	6.137
9	26718	90.95%	7.268	3.742	0.862	0.712	5.602	2968	89.98%	7.418	4.160	0.828	0.781	4.391
10	26712	90.27%	7.515	3.759	0.849	0.693	5.976	2974	90.76%	7.332	4.086	0.856	0.710	5.718

Note: The Ideal value of slope is 1, and the ideal value of intercept is 0. When the values of statistical indicators are close between training results and testing result, the predictions of model are reliable.

659

660



**Table 3: Statistical Indicators Summary of the Leave-One-Out Cross Validation of OK Interpolation**

	Variable	N	R <sup>2</sup>	MRSE	MAE	r	Intercept	Slope	On Point R <sup>2</sup>
Coefficient Interpolation	TrCA of NO <sub>2</sub> Terrain	530	67.54%	8.49E-04	3.81E-04	0.826	-9.31E-05	1.109	99.87%
	Atmospheric Pressure	530	77.99%	0.148	0.079	0.883	0.003	1.021	99.86%
	Temperature	530	60.11%	0.320	0.102	0.778	0.015	1.080	99.91%
	NDVI	530	79.28%	16.815	6.491	0.892	1.065	1.053	99.93%
	Precipitation	530	75.46%	14.210	5.288	0.869	0.682	1.037	99.91%
	PBLH	530	72.38%	0.004	0.002	0.852	0.001	1.054	99.83%
	2016 Year	530	72.38%	0.004	0.002	0.852	0.001	1.054	99.85%
	2017 Year	530	71.89%	3.161	1.378	0.848	0.081	1.021	99.87%
	2018 Year	530	55.09%	6.727	1.986	0.743	0.218	1.009	99.83%
	2019 Year	530	72.50%	3.642	1.555	0.852	0.150	1.028	99.87%
	2020 Year	530	75.28%	3.273	1.443	0.868	0.170	1.013	99.87%
	2021 Year	530	76.82%	3.791	1.643	0.877	0.223	1.029	99.87%
Mean Value Interpolation	Measured Ground-Level NO <sub>2</sub>	530	34.50%	7.773	5.633	0.626	4.505	0.748	98.40%
	TrCA of NO <sub>2</sub> Terrain	530	79.85%	1143.454	738.228	0.896	75.632	0.946	99.59%
	Atmospheric Pressure	530	67.70%	36.269	21.535	0.823	-17.663	1.018	99.79%
	Temperature	530	84.21%	2.597	1.564	0.919	-0.821	1.046	99.92%
	NDVI	530	54.86%	0.095	0.068	0.748	0.059	0.876	99.44%
	Precipitation	530	86.86%	0.022	0.012	0.932	-0.002	1.009	99.94%
	PBLH	530	77.98%	101.276	53.343	0.883	-18.025	1.024	99.91%

663

664

665

## 666 Reference:

- 667 Bechle, M.J., Millet, D.B., & Marshall, J.D. (2015). National Spatiotemporal Exposure  
668 Surface for NO<sub>2</sub>: Monthly Scaling of a Satellite-Derived Land-Use Regression, 2000–  
669 2010. *Environmental Science & Technology*, 49, 12297-12305
- 670 Beckerman, B., Jerrett, M., Brook, J.R., Verma, D.K., Arain, M.A., & Finkelstein, M.M.  
671 (2008). Correlation of nitrogen dioxide with other traffic pollutants near a major  
672 expressway. *Atmospheric Environment*, 42, 275-290
- 673 Beenstock, M., & Felsenstein, D. (2019). *The econometric analysis of non-stationary*  
674 *spatial panel data*. Springer
- 675 Bigdeli, M., Taheri, M., & Mohammadian, A. (2021). Spatial sensitivity analysis of  
676 COVID-19 infections concerning the satellite-based four air pollutants levels.  
677 *International Journal of Environmental Science and Technology*, 18, 751-760
- 678 Breusch, T.S., & Pagan, A.R. (1980). The Lagrange Multiplier Test and its Applications to  
679 Model Specification in Econometrics. *The Review of Economic Studies*, 47, 239
- 680 Brunekreef, B., & Holgate, S.T. (2002). Air pollution and health. *The Lancet*, 360, 1233-  
681 1242
- 682 Brunson, C., Fotheringham, A.S., & Charlton, M.E. (2010). Geographically Weighted  
683 Regression: A Method for Exploring Spatial Nonstationarity. *Geographical Analysis*, 28,  
684 281-298
- 685 Brunson, C., Fotheringham, S., & Charlton, M. (1998). Geographically Weighted  
686 Regression. *Journal of the Royal Statistical Society: Series D (The Statistician)*, 47, 431-  
687 443
- 688 Chi, Y., Fan, M., Zhao, C., Sun, L., Yang, Y., Yang, X., & Tao, J. (2021). Ground-level  
689 NO<sub>2</sub> concentration estimation based on OMI tropospheric NO<sub>2</sub> and its spatiotemporal  
690 characteristics in typical regions of China. *Atmospheric Research*, 264, 105821
- 691 Chiusolo, M., Cadum, E., Stafoggia, M., Galassi, C., Berti, G., Faustini, A., Bisanti, L.,  
692 Vigotti, M.A., Dessì M.P., Cernigliaro, A., Mallone, S., Pacelli, B., Minerba, S., Simonato,  
693 L., & Forastiere, F. (2011). Short-Term Effects of Nitrogen Dioxide on Mortality and  
694 Susceptibility Factors in 10 Italian Cities: The EpiAir Study. *Environmental Health*  
695 *Perspectives*, 119, 1233-1238
- 696 Croissant, Y., & Millo, G. (2008). Panel Data Econometrics in R: The plm Package.  
697 *Journal of Statistical Software*, 27
- 698 Curier, R.L., Kranenburg, R., Segers, A.J.S., Timmermans, R.M.A., & Schaap, M. (2014).  
699 Synergistic use of OMI NO<sub>2</sub> tropospheric columns and LOTOS–EUROS to evaluate the  
700 NO<sub>x</sub> emission trends across Europe. *Remote Sensing of Environment*, 149, 58-69
- 701 Di, Q., Amini, H., Shi, L., Kloog, I., Silvern, R., Kelly, J., Sabath, M.B., Choirat, C.,  
702 Koutrakis, P., Lyapustin, A., Wang, Y., Mickley, L.J., & Schwartz, J. (2020). Assessing  
703 NO<sub>2</sub> Concentration and Model Uncertainty with High Spatiotemporal Resolution across  
704 the Contiguous United States Using Ensemble Model Averaging. *Environmental Science*  
705 *& Technology*, 54, 1372-1384
- 706 Fan, H., Zhao, C., & Yang, Y. (2020). A comprehensive analysis of the spatio-temporal  
707 variation of urban air pollution in China during 2014–2018. *Atmospheric Environment*, 220,  
708 117066
- 709 Fotheringham, A., Brunson, C., & Charlton, M. (2002). *Geographically Weighted*  
710 *Regression: The Analysis of Spatially Varying Relationships*.

711 Fotheringham, A.S., Crespo, R., & Yao, J. (2015). Geographical and Temporal Weighted  
 712 Regression (GTWR). *Geographical Analysis*, 47, 431-452  
 713 Fotheringham, A.S., & Oshan, T.M. (2016). Geographically weighted regression and  
 714 multicollinearity: dispelling the myth. *Journal of Geographical Systems*, 18, 303-329  
 715 Geddes, J.A., Martin, R.V., Boys, B.L., & Van Donkelaar, A. (2016). Long-Term Trends  
 716 Worldwide in Ambient NO<sub>2</sub> Concentrations Inferred from Satellite Observations.  
 717 *Environmental Health Perspectives*, 124, 281-289  
 718 Gollini, I., Lu, B., Charlton, M., Brunsdon, C., & Harris, P. (2015). GWmodel: An R  
 719 package for exploring spatial heterogeneity using geographically weighted models.  
 720 *Journal of Statistical Software*, 63  
 721 Hamra, G.B., Laden, F., Cohen, A.J., Raaschou-Nielsen, O., Brauer, M., & Loomis, D.  
 722 (2015). Lung Cancer and Exposure to Nitrogen Dioxide and Traffic: A Systematic Review  
 723 and Meta-Analysis. *Environmental Health Perspectives*, 123, 1107-1112  
 724 Hu, X., Waller, L.A., Al-Hamdan, M.Z., Crosson, W.L., Estes, M.G., Estes, S.M.,  
 725 Quattrochi, D.A., Sarnat, J.A., & Liu, Y. (2013). Estimating ground-level PM<sub>2.5</sub>  
 726 concentrations in the southeastern U.S. using geographically weighted regression.  
 727 *Environmental Research*, 121, 1-10  
 728 Irie, H., Boersma, K.F., Kanaya, Y., Takashima, H., Pan, X., & Wang, Z.F. (2012).  
 729 Quantitative bias estimates for tropospheric NO<sub>2</sub> columns retrieved from SCIAMACHY,  
 730 OMI, and GOME-2 using a common standard for East Asia. *Atmospheric Measurement*  
 731 *Techniques*, 5, 2403-2411  
 732 Jiang, M., Sun, W., Yang, G., & Zhang, D. (2017). Modelling Seasonal GWR of Daily  
 733 PM<sub>2.5</sub> with Proper Auxiliary Variables for the Yangtze River Delta. *Remote Sensing*, 9,  
 734 346  
 735 Kang, S. (1985). A note on the equivalence of specification tests in the two-factor  
 736 multivariate variance components model. *Journal of Econometrics*, 28, 193-203  
 737 Kasparoglu, S., Incecik, S., & Topcu, S. (2018). Spatial and temporal variation of O<sub>3</sub>, NO  
 738 and NO<sub>2</sub> concentrations at rural and urban sites in Marmara Region of Turkey.  
 739 *Atmospheric Pollution Research*, 9, 1009-1020  
 740 Kim, M., Brunner, D., & Kuhlmann, G. (2021). Importance of satellite observations for  
 741 high-resolution mapping of near-surface NO<sub>2</sub> by machine learning. *Remote Sensing of*  
 742 *Environment*, 264, 112573  
 743 Larkin, A., Geddes, J.A., Martin, R.V., Xiao, Q., Liu, Y., Marshall, J.D., Brauer, M., &  
 744 Hystad, P. (2017). Global Land Use Regression Model for Nitrogen Dioxide Air Pollution.  
 745 *Environmental Science & Technology*, 51, 6957-6964  
 746 Lelieveld, J., Evans, J.S., Fnais, M., Giannadaki, D., & Pozzer, A. (2015). The contribution  
 747 of outdoor air pollution sources to premature mortality on a global scale. *Nature*, 525, 367-  
 748 371  
 749 Li, C., & Managi, S. (2021). Spatial Variability of the Relationship between Air Pollution  
 750 and Well-being. *Sustainable Cities and Society*, 103447  
 751 Li, C., & Managi, S. (2022). Impacts of air pollution on COVID-19 case fatality rate: a  
 752 global analysis. *Environmental Science and Pollution Research*  
 753 Li, J., & Heap, A.D. (2011). A review of comparative studies of spatial interpolation  
 754 methods in environmental sciences: Performance and impact factors. *Ecological*  
 755 *Informatics*, 6, 228-241

756 Li, L., & Wu, J. (2021). Spatiotemporal estimation of satellite-borne and ground-level NO<sub>2</sub>  
 757 using full residual deep networks. *Remote Sensing of Environment*, 254, 112257  
 758 Li, T., Wang, Y., & Yuan, Q. (2020). Remote Sensing Estimation of Regional NO<sub>2</sub> via  
 759 Space-Time Neural Networks. *Remote Sensing*, 12, 2514  
 760 Lin, C.-A., Chen, Y.-C., Liu, C.-Y., Chen, W.-T., Seinfeld, J.H., & Chou, C.C.K. (2019).  
 761 Satellite-Derived Correlation of SO<sub>2</sub>, NO<sub>2</sub>, and Aerosol Optical Depth with  
 762 Meteorological Conditions over East Asia from 2005 to 2015. *Remote Sensing*, 11, 1738  
 763 Liu, L., Zhang, X., Xu, W., Liu, X., Lu, X., Chen, D., Zhang, X., Wang, S., & Zhang, W.  
 764 (2017). Estimation of monthly bulk nitrate deposition in China based on satellite NO<sub>2</sub>  
 765 measurement by the Ozone Monitoring Instrument. *Remote Sensing of Environment*, 199,  
 766 93-106  
 767 Mackerron, G., & Mourato, S. (2009). Life satisfaction and air quality in London.  
 768 *Ecological Economics*, 68, 1441-1453  
 769 Meng, L., Liu, J., Tarasick David, W., Randel William, J., Steiner Andrea, K., Wilhelmsen,  
 770 H., Wang, L., & Haimberger, L. (2021). Continuous rise of the tropopause in the Northern  
 771 Hemisphere over 1980–2020. *Science Advances*, 7, eabi8065  
 772 Newell, K., Kartsonaki, C., Lam, K.B.H., & Kurmi, O.P. (2017). Cardiorespiratory health  
 773 effects of particulate ambient air pollution exposure in low-income and middle-income  
 774 countries: a systematic review and meta-analysis. *The Lancet Planetary Health*, 1, e368-  
 775 e380  
 776 Nickolay, K., Lok, L., Sergey, M., Edward, C., Eric, B., William, S., Joanna, J., & the OMI  
 777 core team (2019). OMI/Aura NO<sub>2</sub> Total and Tropospheric Column Daily L2 Global  
 778 Gridded 0.25 degree x 0.25 degree V3. In N.G.S.F. Center (Ed.): Goddard Earth Sciences  
 779 Data and Information Services Center (GES DISC)  
 780 Ogen, Y. (2020). Assessing nitrogen dioxide (NO<sub>2</sub>) levels as a contributing factor to  
 781 coronavirus (COVID-19) fatality. *Science of The Total Environment*, 726, 138605  
 782 OMI Team (2012). Background information about the Row Anomaly in OMI. In  
 783 Orellano, P., Reynoso, J., Quaranta, N., Bardach, A., & Ciapponi, A. (2020). Short-term  
 784 exposure to particulate matter (PM<sub>10</sub> and PM<sub>2.5</sub>), nitrogen dioxide (NO<sub>2</sub>), and ozone (O<sub>3</sub>)  
 785 and all-cause and cause-specific mortality: Systematic review and meta-analysis.  
 786 *Environment International*, 142, 105876  
 787 Pebesma, E.J. (2004). Multivariable geostatistics in S: the gstat package. *Computers &*  
 788 *Geosciences*, 30, 683-691  
 789 Qin, K., Rao, L., Xu, J., Bai, Y., Zou, J., Hao, N., Li, S., & Yu, C. (2017). Estimating  
 790 Ground Level NO<sub>2</sub> Concentrations over Central-Eastern China Using a Satellite-Based  
 791 Geographically and Temporally Weighted Regression Model. *Remote Sensing*, 9, 950  
 792 Rice, M.B., Ljungman, P.L., Wilker, E.H., Gold, D.R., Schwartz, J.D., Koutrakis, P.,  
 793 Washko, G.R., O'Connor, G.T., & Mittleman, M.A. (2013). Short-Term Exposure to Air  
 794 Pollution and Lung Function in the Framingham Heart Study. *American Journal of*  
 795 *Respiratory and Critical Care Medicine*, 188, 1351-1357  
 796 Schoeberl, M.R., Douglass, A.R., Hilsenrath, E., Bhartia, P.K., Beer, R., Waters, J.W.,  
 797 Gunson, M.R., Froidevaux, L., Gille, J.C., Barnett, J.J., Levelt, P.F., & Decola, P. (2006).  
 798 Overview of the EOS aura mission. *IEEE Transactions on Geoscience and Remote Sensing*,  
 799 44, 1066-1074

Shen, Y., Jiang, F., Feng, S., Zheng, Y., Cai, Z., & Lyu, X. (2021). Impact of weather and emission changes on NO<sub>2</sub> concentrations in China during 2014–2019. *Environmental Pollution*, 269, 116163

Song, W., Jia, H., Huang, J., & Zhang, Y. (2014). A satellite-based geographically weighted regression model for regional PM<sub>2.5</sub> estimation over the Pearl River Delta region in China. *Remote Sensing of Environment*, 154, 1-7

Taylor, R. (1990). Interpretation of the Correlation Coefficient: A Basic Review. *Journal of Diagnostic Medical Sonography*, 6, 35-39

Wang, B., & Chen, Z. (2013). An intercomparison of satellite-derived ground-level NO<sub>2</sub> concentrations with GMSMB modeling results and in-situ measurements – A North American study. *Environmental Pollution*, 181, 172-181

Wu, X., Nethery, R.C., Sabath, M.B., Braun, D., & Dominici, F. (2020). Air pollution and COVID-19 mortality in the United States: Strengths and limitations of an ecological regression analysis. *Science Advances*, 6, eabd4049

Yao, Y., Pan, J., Liu, Z., Meng, X., Wang, W., Kan, H., & Wang, W. (2021). Ambient nitrogen dioxide pollution and spreadability of COVID-19 in Chinese cities. *Ecotoxicology and Environmental Safety*, 208, 111421

Yousefian, F., Faridi, S., Azimi, F., Aghaei, M., Shamsipour, M., Yaghmaeian, K., & Hassanvand, M.S. (2020). Temporal variations of ambient air pollutants and meteorological influences on their concentrations in Tehran during 2012–2017. *Scientific Reports*, 10

Yu, D., Zhang, Y., Wu, X., Li, D., & Li, G. (2021). The varying effects of accessing high-speed rail system on China's county development: A geographically weighted panel regression analysis. *Land Use Policy*, 100, 104935

Zheng, Yang, Wu, & Marinello (2019). Spatial Variation of NO<sub>2</sub> and Its Impact Factors in China: An Application of Sentinel-5P Products. *Remote Sensing*, 11, 1939